Physics of Fluids

RESEARCH ARTICLE | JANUARY 16 2024

Real-time optimization of wing drag and lift performance using a movable leading edge FREE

E. A. R. Camacho ; M. M. da Silva ; A. R. R. Silva ✉ ; F. D. Marques

Check for updates

Physics of Fluids 36, 016128 (2024)
https://doi.org/10.1063/5.0185716

View Online
Export Citation
CrossMark

20 January 2024 21:34:15

Physics of Fluids
Special Topic:
Flow and Civil Structures
Submit Today
AIP Publishing

AIP Publishing

Physics of Fluids **ARTICLE** pubs.aip.org/aip/pof

Real-time optimization of wing drag and lift performance using a movable leading edge

Cite as: Phys. Fluids **36**, 016128 (2024); doi: 10.1063/5.0185716
Submitted: 1 November 2023 · Accepted: 23 December 2023 ·
Published Online: 16 January 2024

E. A. R. Camacho,[1,2] M. M. da Silva,[2] A. R. R. Silva,[1,a)] and F. D. Marques[2]

AFFILIATIONS

[1]Aeronautics and Astronautics Research Center (AEROG), LAETA, University of Beira Interior, Covilhã, Portugal
[2]Laboratory of Dynamics (LABDIN), São Carlos School of Engineering, University of São Paulo, São Carlos, Brazil

[a)]Author to whom correspondence should be addressed: andre@ubi.pt

ABSTRACT

A real-time optimization strategy can provide any system with a considerable boost in performance on the fly, which in real-world applications can be translated to lower energy consumption or higher efficiency. This study investigates the particular case of using real-time optimization to improve wing aerodynamic performance with a dynamically activated deflectable leading edge. Its activation aims to minimize drag and maximize lift and is governed by real-time and gradient-based optimization. An extension to a classic method is suggested to enhance gradient estimation accuracy. Experimental data are obtained at a Reynolds number of 2.0×10^5 with the wing fixed at five positions. For each of these positions, optimal leading-edge deflections are found. The results indicate that deflecting the leading edge has a negligible impact on drag and lift before the stall onset. However, the reduction in the pitching moment cannot be ignored. When the wing is experiencing a proper stall, the movable leading edge yields remarkable enhancements, with the lift being approximately raised by 45% together with a substantial increase in the critical angle of attack. The findings highlight the potential of real-time optimization in experimental aerodynamic studies, reinvigorating its application in improving aircraft performance.

Published under an exclusive license by AIP Publishing. https://doi.org/10.1063/5.0185716

20 January 2024 21:34:15

I. INTRODUCTION

Real-time optimization (RTO) consists of a family of techniques that use online measurements to improve a system's behavior subjected to a set of constraints.[1] The system's dynamics are typically evaluated by defining an objective function that can be manipulated with some inputs. With real-time data, these inputs are swiftly adapted under varying conditions, with the typical goal being maximizing efficiency and responsiveness in dynamic systems.

These concepts can easily be adjusted to countless applications and industries. For instance, real-time optimization can play an important role in improving the operation of systems used in offshore oil rigs,[2] optimally recovering and using the surplus heat generated by various manufacturing and processing plants[3] and enhancing the way a resource is used, for example, when a group of subsystems may consume or supply a common resource.[4] In the particular case of the aerospace industry, we see a swift reframing of aerospace engineering to a data-driven environment coupled with machine learning.[5] Connected to RTO methodologies, inevitable benefits regarding fuel efficiency, safety, and quick adaptation to flight conditions will emerge. RTO has been used in several studies with the intent of improving aircraft performance. Precup *et al.*[6] used a scaled wing model for low-speed wind tunnel tests of real-time optimization-based continuous camber and twist shaping concepts. Later, Nguyen *et al.*[7] conducted a wind tunnel investigation using an identical model to minimize drag through real-time adaptive adjustments. Using a highly flexible wing configuration, the authors achieved a drag reduction close to 10%. Also with drag reduction in mind, Reist *et al.*[8] used existing control surfaces to optimize the performance of a business jet. Their results show that by transferring lift to the fuselage, reductions can be seen in induced, wave, and trim drag.

Similarly, Forte *et al.*[9] used the aspect ratio 13.5 Common Research Model (CRM) with a distributed mini-plain flap system to conduct a real-time drag optimization and maneuver loading alleviation study. The results have shown that at Mach 0.85, this distributed flap system can reduce the drag by 6%. Additionally, real-time optimization can reduce the wing root bending moment by approximately 13% when looking at maneuver loading alleviation. A different yet crucial application in aircraft operations is the optimization of wing geometry while considering some constraints, for instance, ice accretion as Li *et al.*[10] studied, observing that lift could increase 16.5% on an iced airfoil while preserving the cruise aerodynamic performance.

An additional area of study that can hugely benefit from coupling it with RTO is aerodynamic stall. As the airfoil increases its angle of attack, flow instabilities at the upper side of the airfoil start appearing due to the adverse pressure gradient. When the airfoil reaches its critical angle of attack, the flow becomes separated, leading to a decrease in lift and a drastic increase in drag, making this phenomenon undesirable. One common way to mitigate these unwanted effects is to employ some flow control, typically by modifying the airfoil geometry.[11,12] Important to mention that other interesting approaches are also used, for instance, the actuation of synthetic jets on the suction side of the airfoil,[13,14] the usage of plasmas that can mitigate stall effects non-intrusively,[15–17] or even tubercled wings inspired from large aquatic mammals.[18,19] This concept has been coupled with optimization algorithms to improve UAV design and flight performance[20] with optimal geometries increasing the stall angle as well as the lift when compared to a smooth wing.[21]

Focusing on all the possible geometry modifications, one of the most common ways is to direct the attention to the leading-edge geometry. Slats are a much-known example of a device that effectively mitigates stall at high angles of attack. Also, the actuation of the leading edge can provide noise reduction when wings are used as high-lift devices.[22] However, their deployment at lower angles of attack quickly degrades the aerodynamic performance.[23] Others recur to bioinspired solutions, for instance, Gopinathan and Rose,[24] who developed a wing with leading-edge tubercles to delay the stall phenomenon. The same concept was used by Zhang *et al.*[25] to improve wind turbine blade aerodynamics. The leading-edge protuberances proved to be a convincing passive flow control that improved the aerodynamic efficiency up to 11% in the post-stall region. Indeed, Miklosovic *et al.*[26] showed that with these leading-edge structures, the wing would experience softer stall characteristics by maintaining the flow attached. Other bioinspired concepts, such as imitating a bird's cover feathers placed close to the leading edge, have also shown the potential to enhance lift when the airfoil exceeds its critical angle of attack.[27]

However, as mentioned before, the usage of these high-lift devices may affect the aerodynamic performance at lower angles of attack. This problem can be tackled with a continuous morphing strategy, as implemented by Colletti and Ansell,[28] who used a genetic algorithm to design a morphed leading edge for high-lift applications. The authors also add that morphing is used to maximize the presence of laminar flow in cruise flight by removing surface discontinuities. Similarly, Kintscher *et al.*[29] and Monner *et al.*[30] developed morphing leading-edge devices that act as a step-less droop nose device that demonstrates why many works indicate camber morphing as a viable solution to future aerodynamic surfaces.[31]

Anderson *et al.*[32] also studied the leading-edge drooping mechanism and analyzed both drooped and undrooped wings after the critical angle of attack, with the drooped leading edge being more effective at the stall region. A similar study by Chandrasekhara *et al.*[33] demonstrates how a deflected leading edge can control the dynamic stall. The results have shown that the negative peak pitching moment can be reduced considerably together with a 75% reduction in drag. Other authors push the geometrical modifications even further by coupling the movable leading edge with a Coanda-type flap. This was studied by Burnazzi and Radespiel,[34] who, combining these two systems, saw a prominent growth in the critical angle of attack, which in some conditions can go up by 15° while providing extremely high lift coefficients.

Although offering useful and reasonable aerodynamic improvements to these systems, there is a lack of optimal studies. While there are some optimization studies concerning airfoil morphology, these are typically kept in the computational realm and are not conducted in a real-time manner. Finding an experimental study that pursues the optimal use of a wing is fairly rare, as well as searching for an experimental rig coupled with an algorithm that runs in real time, which is even rarer. Hence, to investigate this unexplored subject, the present paper focuses on mitigating the adverse effects of the aerodynamic stall by optimally improving drag and lift generation. To do so, we use the NACA0012-IK30 airfoil (see Fig. 1), which has been proposed, studied, and optimized by us but solely at the lower Reynolds number spectrum.[35–37] This paper presents an experimental investigation of a 2.5 aspect ratio wing at higher Reynolds numbers (order of 10^5) while coupling it with a real-time and free-model optimization algorithm to find optimal leading edge deflections. To accomplish such a task, the paper offers an extension to the dither-free extremum-seeking control approach proposed by Hunnekens *et al.*[38] by introducing the concept of spatial memory.

II. NACA0012-IK30 AIRFOIL: DESCRIPTION AND EXPERIMENTAL APPARATUS

Our proposal aims to mitigate the occurrence of the aerodynamic stall by optimally modifying the airfoil geometry in a real-time strategy. The well-known airfoil NACA0012, often investigated in academic research and aerospace applications, is selected as a case study, although slightly modified. The actual airfoil, denoted as NACA0012-IK30 airfoil, contains two parts separated by a circular gap, enabling the deflection of the frontal part. The frontal part of the airfoil can be deflected by Ω, as depicted in Fig. 1. This figure also shows other important geometric definitions of the airfoil.

By exploring the moving leading-edge concept, the frontal part of the airfoil can be deflected from the leading edge up to the maximum thickness position (30%*c*). Figure 1 also illustrates this capability that can be used to evaluate the impact of the leading edge deflection on the aerodynamic behavior at higher angles of attack.

Force measurements were conducted using a 2.5 aspect ratio wing with a NACA0012-IK30 airfoil. For this evaluation, an experimental rig equipped with a wind tunnel was designed and built at the Laboratory of Dynamics at the São Carlos School of Engineering (EESC/USP). The wind tunnel is a subsonic blower equipped with a sirocco fan (Motovent SVDL-600 model) capable of reaching approximately 27 $\mathrm{m\,s^{-1}}$ with an exit of $0.5 \times 0.5\,\mathrm{m}^2$. A wingspan of 60 cm was mounted vertically in front of the wind tunnel outlet. Figures 2(a) and 2(b) show the CAD project and the experimental apparatus, respectively.

A mechanism, depicted in Fig. 3, is responsible for the leading edge motion. This mechanism can transmit the rotation from the servo

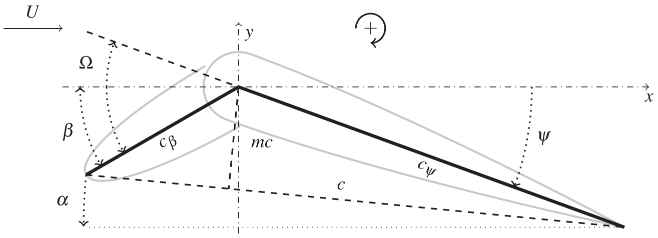

FIG. 1. NACA0012-IK30 wing section.

20 January 2024 21:34:15

Published under an exclusive license by AIP Publishing

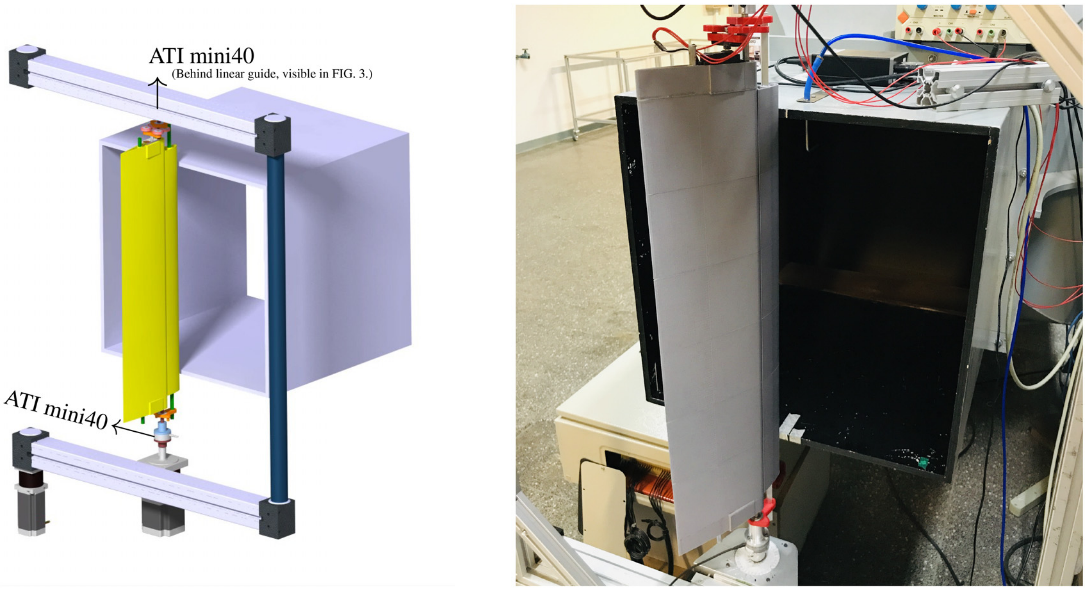

(a) (b)

FIG. 2. CAD project (a) and final assembly (b) of the experimental apparatus for force measurements.

motor axis to the leading edge while keeping the chord's pivot point at 30%*c*. The motor for pitching the leading edge is housed at a particular hub mounted at the wing tip.

The equivalent airspeed (EAS) is measured using a pitot tube placed at the exit section of the wind tunnel, which is connected to a VECTUS TIVA manometer. The true airspeed (TAS) is then obtained by correcting the EAS with the local air density. The temperature and pressure required to calculate the air density are measured using the MT-241A thermo-hygrometer and the VECpress 201 micromanometer. The temperature is also used to calculate the dynamic viscosity using Sutherland's law. Regarding wing positioning control, three motors were used: a stepper motor for transversal adjustments (KTC-HT23-402.8) connected to two linear guides SLDC-60, another to control the angle of attack (KTC-KML093-F07), and a servo motor that handles the movement of the leading edge (SRT DL3017). The servo motor used for the leading-edge pitching is a DC, digital type motor capable of executing a 60° turn from 0.17 to 0.15 s, depending on the operating voltage (4.8–6.0 V). A Simulink model controls all motors via a dSpace DS2101 board running at 1 kHz. The signals are fed to STR8 drivers to control the steppers and to an Arduino board that handles the servo positioning through pulse width modulation.

For force measurements, we use two mini40 force and torque sensors. These are produced by ATI Industrial Automation and come calibrated in advance by the manufacturer with all calibration information loaded on the sensor. Each F/T sensor is connected to an Interface Power Supply (Model IFPS-1 by ATI) from which the transducer's six strain gauge outputs are connected to a dSpace DS2004 board. These are then converted to force and moment data in a Simulink model. The sampling frequency of the F/T sensors is kept the same as the clock frequency set by the Simulink model, at 1 kHz (1 ms). Regarding

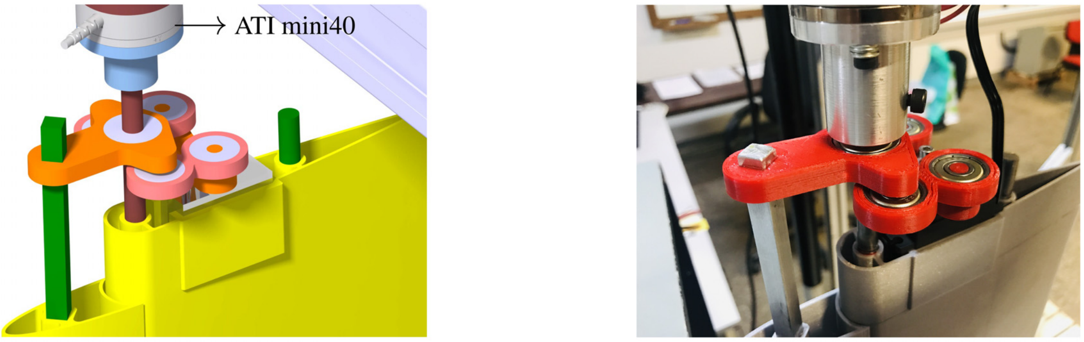

CAD Project **Final Assembly**

FIG. 3. Final assembly of the leading-edge pitching mechanism.

20 January 2024 21:34:15

Published under an exclusive license by AIP Publishing

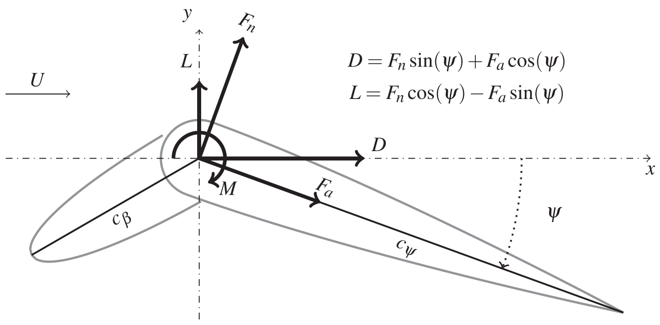

FIG. 4. Sensors positioning and transformation to aerodynamic axis.

measurement uncertainties, all forces and moments are affected by an uncertainty of $\pm 0.5\,\mathrm{N}$ and $\pm 0.03\,\mathrm{N\,m}$, respectively, as indicated by the manufacturer.

The sensors are connected to the main axis at the wing's extremities with the sensor z-axis aligned with the pivot axis of the airfoil, as illustrated in Fig. 4. Since sensors move with the back part, forces are measured at the ψ-part body axis, with F_a and F_n representing the forces in the chordwise and normal-to-chordwise direction.

III. REAL-TIME OPTIMIZATION METHODOLOGY

This section describes a RTO strategy for finding optimal Ω values considering the NACA0012-IK30 wing. This strategy uses a gradient-based and model-free optimization algorithm, which looks at reducing drag and improving the lift coefficients by employing the following function:

$$F = \varphi(-C_D) + (1 - \varphi)C_L, \tag{1}$$

where φ is a weighting factor.

However, one should consider that in a real-time optimization, the experimental setup is susceptible to vibrations, inevitably yielding noisy measurements. These noisy data create an enormous challenge to gradient-based methods, especially gradient evaluation.

The effect of the vibrations and other turbulent-flow-associated effects in the measurements of F can be reduced by considering a moving average of Eq. (1). Therefore, this work follows a stochastic methodology capable of overcoming this issue while following a gradient-based approach by considering the following objective function:

$$\mathcal{O} = \frac{1}{j} \sum_{i=n-j+1}^{n} \varphi(-C_{D_i}) + (1 - \varphi)C_{L_i}, \tag{2}$$

which uses the last j data points. Although force measurements or $\mathcal{O}$ were not conventionally filtered, the moving average effectively acts as a low-pass filter; therefore, j should be chosen to avoid a considerable phase lag between F and $\mathcal{O}$. The objective function $\mathcal{O}$ should be maximized in this proposal. In this way, the solution of this optimization problem is given by

$$\underset{\Omega \in [-40^\circ, 40^\circ]}{\operatorname{argmax}} \quad \mathcal{O}, \tag{3}$$

with the Ω constraints indicating the maximum leading-edge deflection relative to the back part.

Since we are using a gradient approach, the search for a leading-edge position that maximizes $\mathcal{O}$ follows the recursive equation

$$\Omega^{t+1} = \Omega^t + \gamma \frac{\mathrm{d}\mathcal{O}}{\mathrm{d}\Omega}, \tag{4}$$

where γ is the optimization step size and t indicates the time instant. The previous equation can be rewritten as

$$\Delta\Omega = \gamma \frac{\mathrm{d}\mathcal{O}}{\mathrm{d}\Omega}, \tag{5}$$

where $\Delta\Omega = \Omega^{t+1} - \Omega^t$. Equation (5) resembles a P-controller (proportional gain control), where $\Delta\Omega$ is the control output $u(t)$, γ is the proportional gain, and $\mathrm{d}\mathcal{O}/\mathrm{d}\Omega$ is the error.

This work extends this understanding to a broader expression considering the I-controller and D-controller (integral and derivative gain controls). This approach promotes flexibility for this proposal since the integral gain can account for past information while the derivative gain can capture the tendency of the present information. Therefore, the proposal follows a PID (proportional integral differential)-controller framework.

It is well-known that the general control output $u(t)$ of a PID controller is given by

$$u(t) = K_p e(t) + K_i \int_0^t e(t)\mathrm{d}t + K_d \frac{\mathrm{d}e(t)}{\mathrm{d}t}, \tag{6}$$

where K_p, K_i, and K_d are the proportional, integral, and derivative terms. Alternatively, Eq. (6) is rewritten in the following form:

$$u(t) = K_p \left(e(t) + \frac{1}{T_i} \int_0^t e(t)\mathrm{d}t + T_d \frac{\mathrm{d}e(t)}{\mathrm{d}t} \right), \tag{7}$$

where T_i and T_d are the integral and derivative times.

Considering the proposal, the error value is given by

$$e(t) = \frac{\mathrm{d}\mathcal{O}}{\mathrm{d}\Omega}, \tag{8}$$

and the controller output is used as

$$\Omega^{t+1} = \Omega^t + u(t). \tag{9}$$

Krishnamoorthy and Skogestad[39] presented a recent and thorough review of real-time optimization as a feedback control problem. They enumerated several strategies to estimate the gradient, considering model-based and model-free methods. Among the strategies considering model-based methods, there are gradient estimation strategies based on transient measurements, the fast Fourier transform (FFT), the Kalman filter, and the least squares problem. The present work proposes a novel technique using regression techniques and transient measurements. The gradient estimation comprises two parts indicated by the upper indexes: (1) derived using regression techniques and (2) derived using transient measurements.

As mentioned before, the gradient cannot be directly estimated with real-time data due to the presence of noise. Considering this limitation, our proposal first uses an online local linear modeling strategy

20 January 2024 21:34:15

based on the method proposed by Hunnekens *et al.*,[38] who exploit a moving linear regression to estimate the gradient.

In this way, as we run the optimization process, we save the last q ordered pairs $(\Omega, \mathscr{O})$, and for each time step, we use all gathered data to calculate the following linear regression:

$$\hat{\mathscr{O}}^{(1)} = \varepsilon_1 \Omega^* + \varepsilon_0, \tag{10}$$

where the hat ^ and the upper-index (1) indicates an estimated value of $\mathscr{O}$ using regression techniques, $\varepsilon_0, \varepsilon_1$ are the linear-regression parameters obtained using the least squares method, and Ω^* is a perturbed version of Ω to avoid ill-conditioning problems. Using this approach, one can easily obtain an estimate of the gradient given by

$$\frac{\mathrm{d}\hat{\mathscr{O}}^{(1)}}{\mathrm{d}\Omega^*} = \varepsilon_1. \tag{11}$$

One particular problem with this formulation is the fact that if the last q values of Ω are very close or even the same, the calculation of ε_1 can easily become a badly or an ill-conditioned problem, compromising the gradient evaluation. One simple way to mitigate this problem is to randomly perturb each Ω before they enter the regression calculations. The aforementioned modification, Ω^*, is given by

$$\Omega^* = \Omega + U(-\Upsilon, \Upsilon), \tag{12}$$

where $U(-\Upsilon, \Upsilon)$ represents a random number generated by a uniform distribution with values between $-\Upsilon$ and Υ. The Υ value must be chosen to avoid overdamping the gradient evaluation.

Although it is a fairly simple way to estimate the gradient, this dither-free extremum-seeking control approach must be used cautiously since a local model, obtained by evaluating the last q ordered pairs, offers only an approximate representation of the vicinity of $\mathscr{O}$ for a given Ω. This behavior yields a non-trivial relation between the controller gains (K_p, K_p/T_i, K_pT_d) and q. Moreover, the number q must be chosen carefully since a low number of ordered pairs can lead to a noisy gradient estimation. In contrast, too many points will misrepresent the local gradient with data outside the vicinity of Ω^t. One can find further information on these approaches' intricacies and the differences between the dynamic and static map settings at Hunnekens *et al.*[38]

While the method proposed by Hunnekens *et al.*[38] is central to the current RTO methodology, we propose an extension by implementing the concept of spatial memory using transient measurements. In fact, the method has a temporary memory of the last ωq seconds when using a moving linear regression of the previous q data points, where ω is the data acquisition frequency. This means that after ωq seconds, the measurement system retains no information in the Ω domain.

To implement some level of spatial memory, real-time measurements of $\mathscr{O}$ are used to create a static map between the input, Ω, and the objective function. As illustrated in Fig. 5, this is accomplished by the vector $\vec{\mathscr{O}}$ which has 81 elements, effectively dividing the Ω space from $-40°$ to $40°$ with $1°$ intervals.

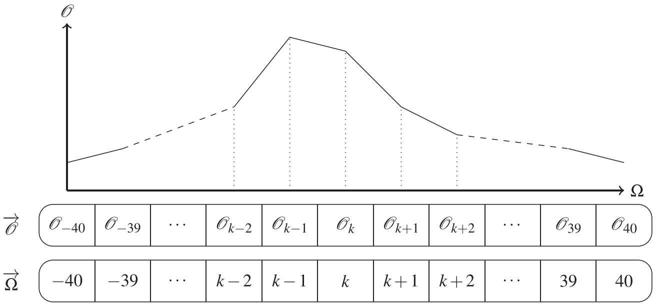

FIG. 5. Static map from transient measurements.

The static map is built by initializing the vector $\vec{\mathscr{O}}$ with a large negative value when the optimization starts. As the algorithm runs, the term $\mathscr{O}_k$ of the vector $\vec{\mathscr{O}}$ is constantly updated with transient measurements according to

$$\mathscr{O}_k = \begin{cases} \mathscr{O}_{\text{previous}} & \text{if } \lfloor \Omega_t \rceil \neq k, \\ 0.5\left(\mathscr{O}_{\text{actual}} + \mathscr{O}_{\text{previous}}\right) & \text{if } \lfloor \Omega_t \rceil = k, \end{cases} \tag{13}$$

which is evaluated recursively at every time step updating the static map.

A limitation of this approach is the fact that to create the static map accurately, the Ω perturbations must occur at a relatively slow rate to guarantee that the entries $(\Omega, \mathscr{O})$ are a viable representation of the steady-state case. In the present study, this is achieved by limiting $\dot{\Omega}$, which is accomplished by saturating the PID output in control terms. Since the output was severely saturated, there was no need to implement the derivative part of the controller, commonly used to dampen the controller response.

This static map is used for deriving the gradient estimation using transient measurements. This second part is computed as

$$\frac{\mathrm{d}\hat{\mathscr{O}}^{(2)}}{\mathrm{d}\Omega} = \begin{cases} \dfrac{\mathscr{O}_t - \max \vec{\mathscr{O}}}{\Omega_t - \operatorname{argmax} \vec{\mathscr{O}}} & \text{if } \Omega_t > \operatorname{argmax} \vec{\mathscr{O}}, \\[2ex] \dfrac{\max \vec{\mathscr{O}} - \mathscr{O}_t}{\operatorname{argmax} \vec{\mathscr{O}} - \Omega_t} & \text{if } \Omega_t < \operatorname{argmax} \vec{\mathscr{O}}, \\[2ex] 0, & \text{if } \Omega_t = \operatorname{argmax} \vec{\mathscr{O}}, \end{cases} \tag{14}$$

which directly connects the current system state to the max $\vec{\mathscr{O}}$.

This approach takes into account recent transient measurements as illustrated in Fig. 6. This figure shows the gradient estimation strategies proposed by Hunnekens *et al.*[38] (left) and the ones proposed in this work (right).

With this framework, the gradient evaluation using both the moving linear regression and the static map maximum is achieved by

$$\frac{\mathrm{d}\mathscr{O}}{\mathrm{d}\Omega} \approx \frac{1}{2}\left(\frac{\mathrm{d}\hat{\mathscr{O}}^{(1)}}{\mathrm{d}\Omega^*} + \frac{\mathrm{d}\hat{\mathscr{O}}^{(2)}}{\mathrm{d}\Omega}\right), \tag{15}$$

which as seen in Fig. 6, will act against the delay introduced by using older data to estimate the true gradient.

Figure 7 illustrates the optimization algorithm that combines the gradient estimations derived by the moving linear regression strategies and by the static map. A pseudocode is described in the Algorithm 1.

20 January 2024 21:34:15

Published under an exclusive license by AIP Publishing

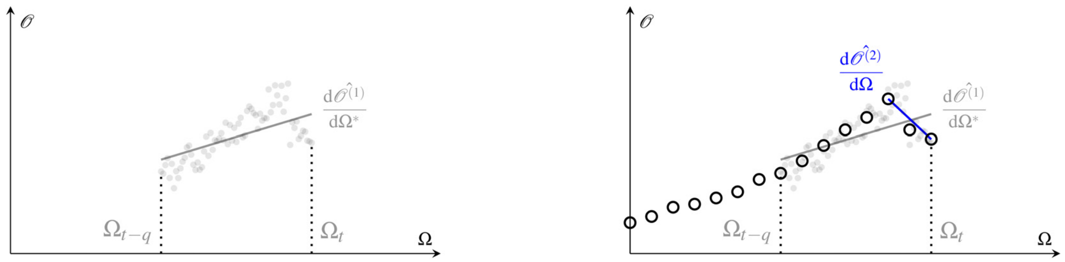

FIG. 6. Optimization framework proposed by Hunnekens *et al.*[38] (left) and the extension proposed in the present work (right).

ALGORITHM 1. RTO algorithm.

```
while RTO is activated do
    Update the delay vector with the latest measurement $[Z_t^{-1}, Z_{t-1}^{-1}, Z_{t-2}^{-1}, \ldots, Z_{t-q}^{-1}]$.
    Update the static map, $\mathscr{O}^{(2)}$, using Eq. (13).
    Compute the moving linear regression of the delay vector, $\hat{\mathscr{O}}^{(1)}$, using Eq. (10).
    Determine first gradient estimation, $\varepsilon_1$, using Eq. (11).
    Locate the max and argmax of the static map.
    Compute the second gradient estimation based on the static map, using Eq. (14).
    Determine the final gradient estimate with Eq. (15).
    Feed the gradient estimate to the PID controller, obtaining $u$ as seen in Eq. (7).
    Update the leading edge deflection using Eq. (9).
end while
```

Regarding the initial values of the PID gains, we derived them using the Ziegler–Nichols tuning method.[40] Further adjustments were made to achieve an acceptable response, where the maximum is reached somewhat quickly. All parameters used for the optimization using the local linear static model are presented in Table I. These were tested and calibrated when analyzing the NACA0012-IK30 at $Re = 3.0 \times 10^5$ and $\psi = 30°$.

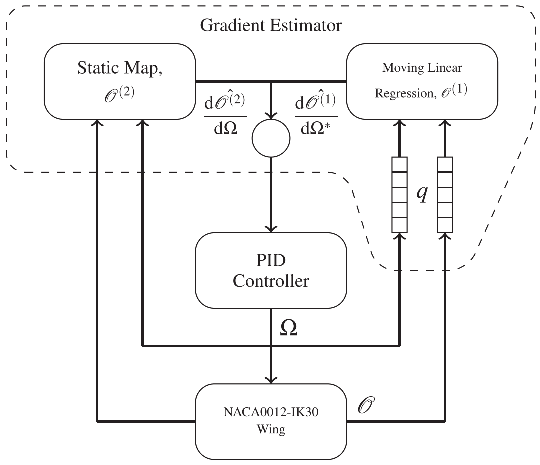

FIG. 7. RTO formulation.

IV. RESULTS AND DISCUSSION

In this section, the results from the implementation of the RTO methodology are presented. The optimization consists of studying the NACA012-IK30 wing at a Reynolds number of $Re = 3.0 \times 10^5$ with five different ψ, 10°, 15°, 20°, 25°, and 30°. Based on the objective function, $\mathscr{O}$, the real-time optimization will look into the minimization of drag ($\varphi = 1$) and the maximization of lift ($\varphi = 0$). Additionally, the influence of the leading edge position on the moment coefficient and aerodynamic efficiency, C_L/C_D, is presented.

The optimization process starts with the airfoil at $\alpha = \psi$, meaning that there is no leading edge deflection ($\Omega = 0°$). Then, it runs for 60 s, meaning that max $\mathscr{O}$ is expected to be reached in under 1 min, although it is typically quicker, as seen in the results. Force measurements start at $t = -5$ s but the optimization only starts when $t = 0$ s. The first 5 s are used as a reference to calculate relative improvements.

The analysis starts by presenting the real-time minimization of drag, shown in Fig. 8. The drag coefficient and the airfoil angle of attack are plotted side by side as a function of time for the five ψ cases.

Starting with $\psi = 10°$, the optimization results in a constant drag coefficient over time, indicating that the search was initiated closer to the minimum. In fact, at $\alpha = 10°$, the airfoil is not expected to experience significant flow separation, a condition in which moving the leading edge does not bring any considerable benefit. This changes with $\psi = 15°$, where the optimization process finds a lower drag condition. Yet, the reduction is not as significant as in the following conditions. When ψ is set at 20°, the wing is already undergoing extensive stall. In these conditions, the movable leading edge shows its real potential.

TABLE I. Parameters for the optimization of the NACA0012-IK30 wing.

Simulink model clock	ω_{Simulink}	1 kHz
Moving average window	j	1000 samples (1 s)
Proportional gain	K_p	1.000
Integral gain	K_i	0.100 ($T_i = 10$ s)
Derivative gain	K_d	0.000 ($T_d = 0$ s)
Maximum Ω deflection	max Ω	$\pm 40°$
Maximum $\dot{\Omega}$	max $\dot{\Omega}$	$\pm 2°\ \text{s}^{-1}$
Anti-windup scheme	…	Clamping
Delay vector size	q	5000 samples (5 s)
Random perturbation parameter	Υ	0.1°

20 January 2024 21:34:15

Published under an exclusive license by AIP Publishing

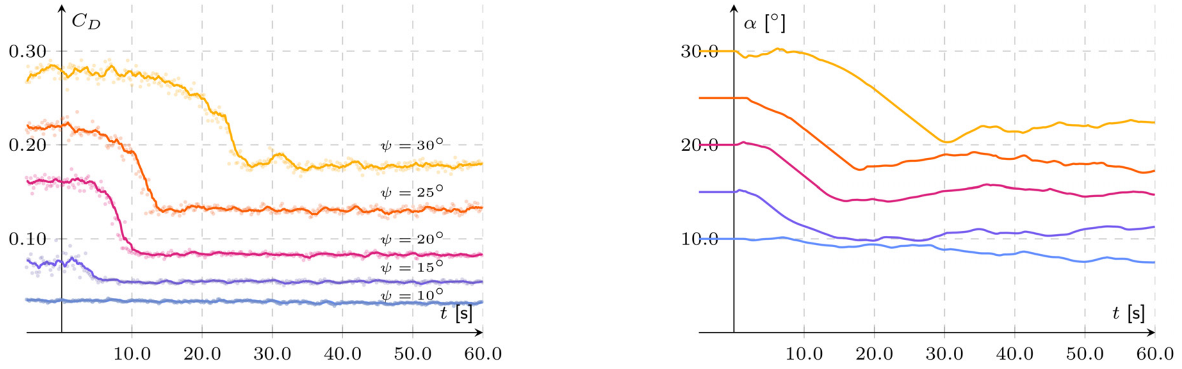

FIG. 8. RTO of drag: Drag coefficient (left) and wing's angle of attack (right).

As a matter of fact, the real-time optimization provides a substantial reduction in drag, bringing the wing to the drag level experienced when at $\alpha = 15°$ and $\Omega = 0°$.

These improvements happen due to the following physical phenomena. When $\psi = 20°$, as mentioned above, the wing is at its stall region, meaning that the airflow on its surface was subjected to an adverse pressure gradient strong enough to reverse the flow direction. With $\psi = 15°$ the effects were not as visible since a substantial stall had not been reached yet. As soon as the RTO starts, and the downward motion of the leading edge is detected as advantageous, the suction peak and adverse pressure gradient start becoming less intense. It is important to highlight that lowering β yields changes in the wing's curvature and angle of attack. All these combined lead to the flow becoming more attached, reducing the wake and, therefore, reducing drag.

With $\psi = 25°$ and 30°, identical effects are identified, with the latter case being able to go down as close as to when the airfoil is at 20° with no leading edge deflection. Looking at the evolution of the wing angle of attack, it is clear that the leading edge position converges to an interval rather than to a definite value. This is justified first by the noisy measurements that induce oscillations to the gradient estimate but also due to the existence of drag buckets in the β domain, as will be seen when plotting C_D against the leading edge angle of attack.

Regarding the optimization of the lift coefficient, presented in Fig. 9, the movable leading edge shows its prospect of improving lift generation when the airfoil is in a deep stall.

Similarly, the drag minimization, when $\psi = 10°$, deflecting the leading edge holds no considerable effect. The same is seen with $\psi = 15°$, and although the angle of attack changes over time for these two cases, as seen on the right graph, the lift coefficient remains fairly constant. For the next three conditions ($\psi = 20°$, 25°, and 30°), the wing starts the optimization with similar lift coefficients, which indicates that the onset of the stall is somewhere close to 15°. Once again, a singular angle of attack cannot be reached as the gradient estimation is bumpy, but the control is still strong enough to keep the wing at a high lift level.

Similar to the drag minimization runs, as the leading edge finds its optimal way downward, each condition branches out into various lift coefficients, which result from the flow reattaching to the wing as the adverse pressure gradients become less intense. This lift increase is also accompanied by a drag reduction, a typical characteristic of mitigating or recovering from a stall. As seen ahead, these two effects combined will offer a noticeable aerodynamic efficiency boost.

In contrast to the previous graph, Fig. 10 shows the optimization process's history against the leading-edge attack angle, β, for both C_D and C_L. These graphs show the point cloud measured during the RTO together with the static map built during the optimization for all ψ cases. Looking at $\psi = 10°$, both drag and lift coefficients start at flat and wide regions where the gradient is close to zero. The fluctuations during the gradient estimation process make the leading edge go search away from $\beta = 10°$ but have shown no influence in the

20 January 2024 21:34:15

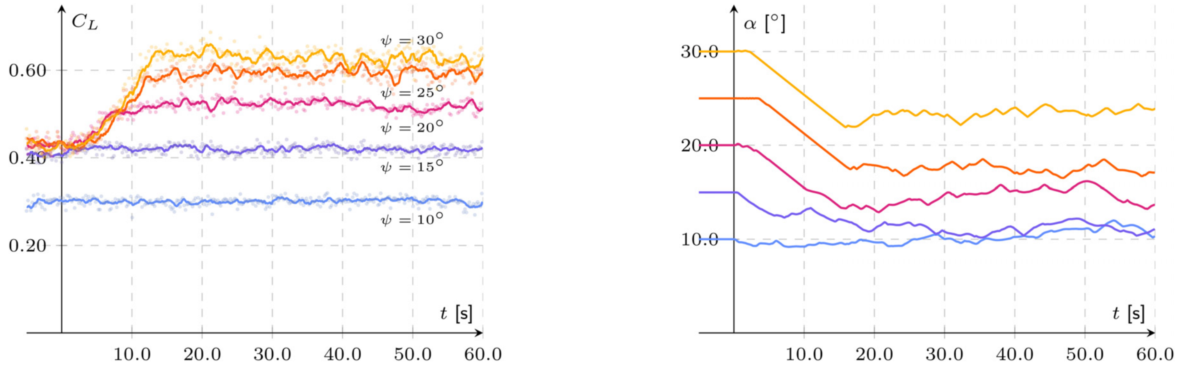

FIG. 9. RTO of lift: Lift coefficient (left) and wing's angle of attack (right).

Published under an exclusive license by AIP Publishing

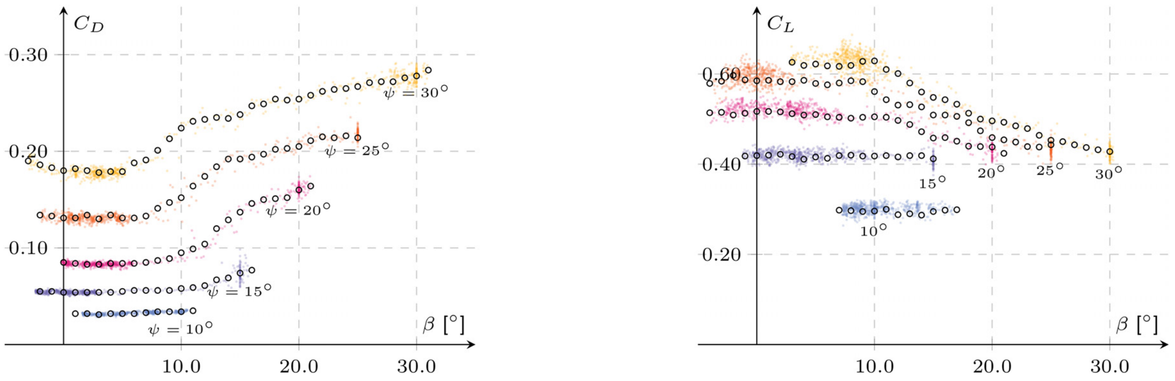

FIG. 10. Drag minimization (left) and lift maximization (right) in the β domain.

gradient, indicating that we started very close to minimal drag and maximum lift coefficients. The same is seen for the lift coefficient when $\psi = 15°$ but not for drag. As observed on the left graph, the overall airfoil benefits from a β reduction, indicating that some flow separation is present and that lowering the leading edge may reduce or eliminate it. For the last three cases, $\psi = 20°$, 25°, and 30°, a similar behavior is seen. The drag coefficient starts relatively high, as expected in these angles of attack, and starts decreasing as β drops. In these cases, somewhere between 8° and 13°, a rapid drag reduction is observed, which can mainly be justified by a significant flow reattachment on the wing surface. The lift does not exhibit the same behavior on the right graph, growing steadily as the leading edge pitches down. Similar to the drag coefficient, the optimization finds a wide region of maximum lift instead of a single point.

To summarize the optimization results, Fig. 11 presents the relative improvements obtained from the RTO implementation. Both graphs present the wing with no leading edge deflection ($\Omega = 0°$) and the optimal leading edge position found for both drag and lift coefficients. The calculations were made by averaging the first and last 5 s of the experiment and calculating their relative variation. Regarding drag generation, it is observed that by just deflecting the leading edge, great improvements can be achieved with drag reductions that can go near 47%. Its true potential is seen at higher angles of attack where extreme flow separation is present. This is also verified for lift production, which sees its maximum gain at $\psi = 30°$ with an increase in 45%. Additionally, something unique is the fact that it is capable of not only enhancing lift but also delaying the onset of stall. When looking at the $\Omega = 0°$ curve, where there is no leading edge deflection, the onset of stall starts around $\alpha = 15°$ where a stagnation is seen in the lift coefficient rise. By using the optimal leading edge position, the onset of the stall is pushed to higher angles of attack while providing much higher lift coefficients, adding enormous flexibility to this modified NACA0012 wing.

Even though the optimization was focused on drag and lift forces, it is also important to analyze how other parameters are affected by the moving leading edge. Figure 12 shows the moment coefficient and aerodynamic efficiency as a function of β using data from both the drag minimization and maximization of C_L.

Looking at the moment coefficient for the $\psi = 10°$, we observe that moving the leading edge has a linear influence on the pitching moment, which does not occur for the other cases. With $\psi = 15°$, a nonlinear behavior is detected close to $\beta = 15°$ where the moment slightly increases as the leading-edge pitches down. Revisiting Fig. 10, this slight increase was accompanied by a reduction in drag. This becomes much more evident when $\psi = 20°$, where reducing the leading edge angle of attack increases the moment initially. This increase is justified by a flow reattachment, which inevitably reduces drag and increases lift, ending up pushing the center of pressure forward and increasing the pitching moment. However, as the leading edge continues to go down, the center of pressure will travel downstream since the suction zone located at the leading edge will lose its density. This leads to the pitching moment reduction when β is less than 10°. With $\psi = 25°$ and 30°, the effects are similar, but the data show an interesting particularity. In these cases, it is clear that before there is an increase in

20 January 2024 21:34:15

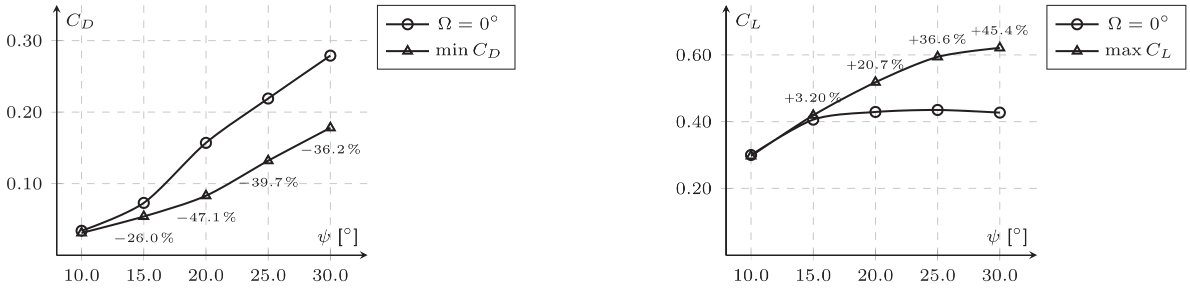

FIG. 11. Drag minimization (left) and lift maximization (right).

Published under an exclusive license by AIP Publishing

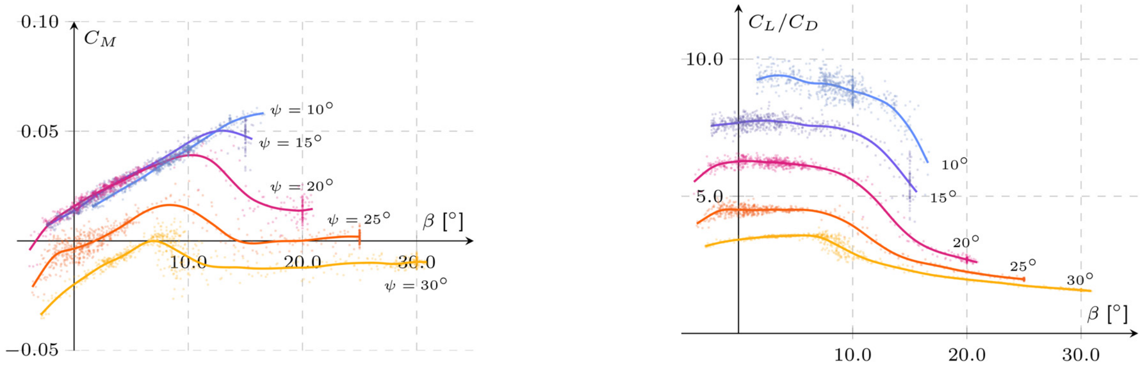

FIG. 12. Moment coefficient at 0.3*c* (left) and aerodynamic efficiency (right).

the moment as β goes down, the wing has a flat region where the moment is not affected even with drag and lift changing. This indicates that the wing's aerodynamic center is very close to the pivot point, where the sensors are positioned.

Concerning aerodynamic efficiency, regardless of the ψ condition, the influence of the leading edge angle of attack is the same, offering considerable improvements relative to the $\Omega = 0°$ configuration. As expected, increasing ψ decreases the lift-to-drag ratio, yet the graph indicates that using the leading edge angle of attack as a variable can mitigate its effects. Indeed, one can achieve higher aerodynamic efficiency than a lower ψ case with the advantage of producing more lift. For instance, the wing at $\psi = 20°$ with optimal β produces more lift and has similar efficiency than when the wing is at $\psi = 10°$ and $\Omega = 0°$.

V. CONCLUSIONS

Applying real-time optimization to engineering problems brings inevitable improvements in the systems' efficiency and/or power consumption. Optimization can play an important role in improving the aerodynamic performance of wings for particular aerospace applications. The present work leaned over this exact topic, where we used a modified version of the conventional NACA0012 airfoil, the NACA0012-IK30 airfoil, coupled with an RTO strategy to mitigate the adverse effects of stall.

This modification consisted of dividing the airfoil into two parts, creating a deflectable leading edge that can be activated dynamically. In this paper, its activation pursues either the minimization of drag or the maximization of lift when the airfoil is at relatively high angles of attack, using a real-time gradient-based optimization. Although not the central part, the paper also offered an extension to the extremum-seeking control using first-order least squares fits for gradient estimation proposed by Hunnekens *et al.*[38] This extension provides the advantages of combating the lag associated with using older data and the fact that, after the optimization process is finished, we obtain an accurate static map that can be used in further modeling.

The experimental study was conducted at a Reynolds number of 3.0×10^5 using a 2.5 aspect ratio wing with the NACA0012-IK30 airfoil. The wing was fixed at five different positions ($\psi = 10°$, 15°, 20°, 25°, and 30°), and for each, a leading-edge deflection is optimally found. The results showed that deflecting the leading edge did not significantly affect drag or lift forces until the stall onset, at around $\psi = 15°$. The same cannot be said for the pitching moment, which exhibits a considerable modification due to the shift of the suction peak. For ψ positions where the wing is truly stalled, the leading edge deflections found by the real-time optimization provide impressive improvements, with drag being reduced down to 47% and lift going up by approximately 45%, which together offer enhanced lift-to-ratios. Additionally, the deflection of the leading edge showed that when used optimally, this leading edge device can push the critical angle of attack to extremely high values.

The results in this paper should revitalize the use of real-time optimization in the context of experimental studies of aerodynamic geometries. Although there are some published developments regarding this topic, there is still a lack of investigation on optimizing on-the-spot aerodynamic surfaces. The proposed geometry could also open ways to straightforward applications in unmanned and light aircraft without deep and complex fatigue phenomena that occur with emerging morphing technologies. As demonstrated, coupling it with an RTO strategy will only add flexibility and reliability to the assigned mission.

ACKNOWLEDGMENTS

The present work was performed under the scope of the Aeronautics and Astronautics Research Center (AEROG) of the Laboratório Associado em Energia, Transportes e Aeronáutica (LAETA) activities, and it was supported by Fundação para a Ciência e Tecnologia (FCT) through Project Nos. UIDB/50022/2020, UIDP/50022/2020, and LA/P/0079/2020 and the grant sponsored by Fundação para a Ciência e Tecnologia 2020.04648.BD. F. D. Marques and M. M. da Silva acknowledge the financial support of the Brazilian National Council for Scientific and Technological Development (CNPq Grant Nos. 306824/2019-1 and #303884/2021-5).

AUTHOR DECLARATIONS

Conflict of Interest

The authors have no conflicts to disclose.

Author Contributions

Emanuel A. R. Camacho: Conceptualization (equal); Formal analysis (equal); Investigation (equal); Methodology (equal); Project

20 January 2024 21:34:15

Published under an exclusive license by AIP Publishing

administration (equal); Software (equal); Visualization (equal); Writing – original draft (equal). **Maíra Martins da Silva:** Conceptualization (equal); Formal analysis (equal); Methodology (equal); Resources (equal); Writing – review & editing (equal). **André Resende Rodrigues Silva:** Conceptualization (equal); Funding acquisition (equal); Methodology (equal); Supervision (equal); Writing – review & editing (equal). **Flavio Marques:** Conceptualization (equal); Funding acquisition (equal); Methodology (equal); Project administration (equal); Resources (equal); Supervision (equal); Writing – review & editing (equal).

DATA AVAILABILITY

The data that support the findings of this study are available from the corresponding author upon reasonable request.

REFERENCES

[1] F. Serralunga, M. C. Mussati, and P. A. Aguirre, "An alternative real-time optimization algorithm with modifier adaptation," in *Computer Aided Chemical Engineering* (Elsevier, 2012), pp. 367–371.

[2] P. de Azevedo Delou, J. Matias, J. Jäschke, M. B. de Souza, and A. R. Secchi, "Steady-state real-time optimization using transient measurements and approximated Hammerstein dynamic model: A proof of concept in an experimental rig," J. Process Control **132**, 103111 (2023).

[3] D. Krishnamoorthy, "Optimizing surplus heat recovery using fast Fourier transform-based extremum seeking control," IFAC-PapersOnLine **56**, 7178–7183 (2023).

[4] D. Krishnamoorthy, "A distributed feedback-based online process optimization framework for optimal resource sharing," J. Process Control **97**, 72–83 (2021).

[5] S. L. Brunton, J. N. Kutz, K. Manohar, A. Y. Aravkin, K. Morgansen, J. Klemisch, N. Goebel, J. Buttrick, J. Poskin, A. W. Blom-Schieber, T. Hogan, and D. McDonald, "Data-driven aerospace engineering: Reframing the industry with machine learning," AIAA J. **59**, 2820–2847 (2021).

[6] N. Precup, M. Mor, and E. Livne, "An active variable camber continuous trailing edge flapped wing wind tunnel model for aeroelastic 'In-Flight' shape optimization tests," AIAA Paper No. 2018-3106, 2018.

[7] N. T. Nguyen, N. B. Cramer, K. E. Hashemi, E. Ting, M. Drew, R. Wise, J. Boskovic, N. Precup, T. Mundt, and E. Livne, "Real-time adaptive drag minimization wind tunnel investigation of a flexible wing with variable camber continuous trailing edge flap system," AIAA Paper No. 2019-3156, 2019.

[8] T. A. Reist, D. Koo, and D. W. Zingg, "Aircraft cruise drag reduction through variable camber using existing control surfaces," J. Aircr. **59**, 1406–1415 (2022).

[9] C. Forte, N. T. Nguyen, J. Xiong, and J. Sager, "Real-time drag optimization and maneuver load alleviation control for a high aspect ratio wing wind tunnel model," AIAA Paper No. 2022-0715, 2022.

[10] H. Li, Y. Zhang, and H. Chen, "Optimization of supercritical airfoil considering the ice-accretion effects," AIAA J. **57**, 4650–4669 (2019).

[11] R. Wang, X. Ma, G. Zhang, P. Ying, and X. Wang, "Numerical simulation of continuous morphing wing with leading edge and trailing edge parabolic flaps," J. Aerosp. Eng. **36**, 04023051 (2023).

[12] M. Jentys and C. Breitsamter, "Aerodynamic drag reduction through a hybrid laminar flow control and variable camber coupled wing," Aerosp. Sci. Technol. **142**, 108652 (2023).

[13] S. A. Tran, A. Fisher, D. A. Corson, and O. Sahni, "Dynamic stall alleviation for an SC1095 airfoil using synthetic jets," AIAA Paper No. 2015-1038, 2015.

[14] R. Duvigneau and M. Visonneau, "Optimization of a synthetic jet actuator for aerodynamic stall control," Comput. Fluids **35**, 624–638 (2006).

[15] T. C. Corke, M. L. Post, and D. M. Orlov, "SDBD plasma enhanced aerodynamics: Concepts, optimization and applications," Prog. Aerosp. Sci. **43**, 193–217 (2007).

[16] A. Starikovskiy, K. Meehan, N. Persikov, and R. Miles, "Static and dynamic stall control by NS SDBD actuators," Plasma Sources Sci. Technol. **28**, 054001 (2019).

[17] H. Zong, Y. Wu, H. Liang, and Z. Su, "Experimental investigation and intelligent optimization of airfoil zero-lift drag reduction with plasma actuators," AIAA J. **61**, 223–240 (2023).

[18] M. Zhao, L. Xu, Z. Tang, X. Zhang, B. Zhao, Z. Liu, and Z. Wei, "Onset of dynamic stall of tubercled wings," Phys. Fluids **33**, 081909 (2021).

[19] M. Zhao, L. Xu, X. Li, Y. Zhao, and Z. Liu, "Dynamic stall of pitching tubercled wings in vortical wake flowfield," Phys. Fluids **35**, 015122 (2023).

[20] K. Arunkumar, G. Sravanthi, A. U. Deepika, and M. Srikanth, "Optimization of UAV by using tubercles wing configuration," AIP Conf. Proc. **2492**, 020018 (2023).

[21] Y. Lu, Z. Li, X. Chang, Z. Chuang, and J. Xing, "An aerodynamic optimization design study on the bio-inspired airfoil with leading-edge tubercles," Eng. Appl. Comput. Fluid Mech. **15**, 292–312 (2021).

[22] G. Chen, B. Chen, X. Yang, X. Tang, J. Ding, and P. Weng, "Noise reduction for high-lift devices on a swept wing model by droop nose," Aerosp. Sci. Technol. **143**, 108702 (2023).

[23] M. A. R. Mohamed, K. S. K. Reddy, and S. S. S. Vishnu, "Bio-inspired optimization of leading edge slat," Aircr. Eng. Aerosp. Technol. **95**, 725–733 (2022).

[24] V. T. Gopinathan and J. B. R. Rose, "Aerodynamic performance characterization of bio-inspired wings with leading edge tubercles at low Reynolds number," Proc. Inst. Mech. Eng., Part G **237**, 561–586 (2022).

[25] Y. Zhang, M. Zhao, and M. Zhang, "Research on the aerodynamic performance of the wind turbine blades with leading-edge protuberances," Ocean Eng. **280**, 114615 (2023).

[26] D. S. Miklosovic, M. M. Murray, and L. E. Howle, "Experimental evaluation of sinusoidal leading edges," J. Aircr. **44**, 1404–1408 (2007).

[27] D. O. D. Izquierdo and F. D. Marques, "Experimental analysis of passive bio-inspired covert feathers for stall and post-stall performance enhancement," Meccanica **56**, 2671–2689 (2021).

[28] C. R. Colletti and P. J. Ansell, "Airfoil morphed leading-edge design for high-lift applications using genetic algorithm," J. Aircr. **60**, 160–171 (2023).

[29] M. Kintscher, M. Wiedemann, H. P. Monner, O. Heintze, and T. Kühn, "Design of a smart leading edge device for low speed wind tunnel tests in the European project SADE," Int. J. Struct. Integr. **2**, 383–405 (2011).

[30] H. Monner, M. Kintscher, T. Lorkowski, and S. Storm, "Design of a smart droop nose as leading edge high lift system for transportation aircrafts," AIAA Paper No. 2009-2128, 2009.

[31] R. J. Raj and J. B. R. Rose, "Flow physics and boundary layer optimization over a NACA airfoil by camber morphing at subsonic speeds," Int. J. Mod. Phys. C **34**, 2350080 (2022).

[32] J. D. Anderson, S. Corda, and D. M. V. Wie, "Numerical lifting line theory applied to drooped leading-edge wings below and above stall," J. Aircr. **17**, 898–904 (1980).

[33] M. S. Chandrasekhara, P. B. Martin, and C. Tung, "Compressible dynamic stall control using a variable droop leading edge airfoil," J. Aircr. **41**, 862–869 (2004).

[34] M. Burnazzi and R. Radespiel, "Design and analysis of a droop nose for coanda flap applications," J. Aircr. **51**, 1567–1579 (2014).

[35] E. A. Camacho, A. R. Silva, and F. D. Marques, "Optimal operation of the NACA0012-IK30 airfoil," AIAA Paper No. 2023-4439, 2023.

[36] E. A. R. Camacho, F. D. Marques, and A. R. R. Silva, "Influence of a deflectable leading-edge on a flapping airfoil," Aerospace **10**, 615 (2023).

[37] E. A. Camacho, A. R. Silva, and F. D. Marques, "Optimal leading-edge deflection for flapping airfoil propulsion," Proc. Inst. Mech. Eng., Part G **237**, 3640–3653 (2023).

[38] B. Hunnekens, M. Haring, N. van de Wouw, and H. Nijmeijer, "A dither-free extremum-seeking control approach using 1st-order least-squares fits for gradient estimation," in *53rd IEEE Conference on Decision and Control* (IEEE, 2014).

[39] D. Krishnamoorthy and S. Skogestad, "Real-time optimization as a feedback control problem—A review," Comput. Chem. Eng. **161**, 107723 (2022).

[40] J. G. Ziegler and N. B. Nichols, "Optimum settings for automatic controllers," J. Dyn. Syst., Meas., Control **115**, 220–222 (1993).

20 January 2024 21:34:15

Published under an exclusive license by AIP Publishing